Draft version May 24, 2022
Preprint typeset using LaTeX style AASTeX6 v. 1.0

arXiv:1712.05509v1 [astro-ph.SR] 15 Dec 2017

AN OPTICAL AND INFRARED TIME-DOMAIN STUDY OF THE SUPERGIANT FAST X-RAY TRANSIENT CANDIDATE IC 10 X-2

Stephanie Kwan[1], Ryan M. Lau[1], Jacob Jencson[1], Mansi M. Kasliwal[1], Martha L. Boyer[2,3], Eran Ofek[4], Frank Masci[5], Russ Laher[5]

[1]Division of Physics, Mathematics and Astronomy, California Institute of Technology (Caltech), 1200 E. California Blvd., Pasadena, CA 91125 USA
[2]Observational Cosmology Lab, Code 665, NASA Goddard Space Flight Center, Greenbelt, MD 20771 USA
[3]Oak Ridge Associated Universities (ORAU), Oak Ridge, TN 37831 USA
[4]Department of Particle Physics and Astrophysics, Weizmann Institute of Science, Rehovot 76100, Israel
[5]Infrared Processing and Analysis Center, Caltech, 1200 E. California Blvd., Pasadena, CA 91125 USA

ABSTRACT

We present an optical and infrared (IR) study of IC 10 X-2, a high-mass X-ray binary in the galaxy IC 10. Previous optical and X-ray studies suggest X-2 is a Supergiant Fast X-ray Transient: a large-amplitude (factor of ~ 100), short-duration (hours to weeks) X-ray outburst on 2010 May 21. We analyze R- and g-band light curves of X-2 from the intermediate Palomar Transient Factory taken between 2013 July 15 and 2017 Feb 14 show high-amplitude ($\gtrsim 1$ mag), short-duration ($\lesssim 8$ d) flares and dips ($\gtrsim 0.5$ mag). Near-IR spectroscopy of X-2 from Palomar/TripleSpec show He I, Paschen-γ, and Paschen-β emission lines with similar shapes and amplitudes as those of luminous blue variables (LBVs) and LBV candidates (LBVc). Mid-IR colors and magnitudes from *Spitzer*/IRAC photometry of X-2 resemble those of known LBV/LBVcs. We suggest that the stellar companion in X-2 is an LBV/LBVc and discuss possible origins of the optical flares. Dips in the optical light curve are indicative of eclipses from optically thick clumps formed in the winds of the stellar counterpart. Given the constraints on the flare duration ($0.02 - 0.8$ d) and the time between flares (15.1 ± 7.8 d), we estimate the clump volume filling factor in the stellar winds, f_V, to be $0.01 < f_V < 0.71$, which overlaps with values measured from massive star winds. In X-2, we interpret the origin of the optical flares as the accretion of clumps formed in the winds of an LBV/LBVc onto the compact object.

1. INTRODUCTION

High-mass X-ray binaries (HMXBs) are accretion-powered binary systems consisting of a neutron star (NS) or black hole accreting matter from its companion high-mass star ($> 10 M_\odot$). HMXBs are historically divided into two classes based on their method of accretion: BeXBs, which accrete from circumstellar disks around an emission-line B (Be) donor star, and supergiant HMXBs (sgHMXBs), which have Roche lobe overflow or stellar winds from an early spectral type supergiant OB donor stars (see Chaty 2014 for a review).

Since its launch in 2002, *INTEGRAL* has led to the discovery of a subclass of sgHMXBs called supergiant fast X-ray transients (SFXTs). SFXTs exhibit unusually high-amplitude (~ 1000), bright ($\sim 10^{36}$-10^{37} erg s^{-1}), fast (minutes to days) outbursts compared to those of regular sgHMXB (Ducci et al. 2014). These outbursts are inconsistent with orbital motion of the neutron star through a smooth medium. Several accretion models have been proposed. One group of models attributes the outbursts with accretion of denser "clumps" in a inhomogeneous, anisotropic stellar wind (e.g. Sidoli et al. 2007; Walter & Zurita Heras 2007; Negueruela et al. 2008). Another group involves accretion-gating mechanisms, where variations in accretion onto the compact object arise from transition stages between magnetic and centrifugal barriers (see Illarionov & Sunyaev 1974; Bozzo, Falanga, & Stella 2008; Drave et al. 2014 and references within). Liu et al. (2001) suggests that some wind-fed sgHMXBs evolved from BeHMXBs, but the relationship between SFXTs and sgHMXBs remains unclear.

Laycock et al. (2014) reported the discovery of IC 10 X-2, another HMXB, based on Chandra measurements of X-ray outbursts in 2003 and 2010. The aspect corrected coordinates for IC 10 X-2 are RA: $00^h20^m20^s.94$, Dec: $59°17^m59^s.0$, with a 95% confidence region of radius 0.6". It was reported to exhibit an X-ray outburst with peak luminosity 1.8×10^{37}erg s^{-1} for the best-fitting power-law spectral model. A second outburst in 2010

May (MJD 55337.5) was constrained to have a duration less than 3 months. Based on IC 10 X-2's X-ray and optical spectra, Laycock et al. (2014) posited that its primary star is a nitrogen-enriched B supergiant star, calling it a "luminous blue supergiant". The B-type supergiant appearance opens the question of whether the primary star is a luminous blue variable (LBV).

LBVs are massive evolved stars that exhibit extreme luminosities ($\sim 10^5 - 10^6$ $L_\odot$), strong spectral variability ($T_{\rm eff} \sim 7000 - 20000$ K), and eruptive mass loss as high as ~ 1 $M_\odot$ yr^{-1} on decade-long timescales (Smith 2014). LBVs, however, are difficult to classify due to the range of spectroscopic and photometric properties that they span.

In order to investigate the nature of IC 10 X-2, we study its optical and IR counterpart using data from the intermediate Palomar Transient Factory (iPTF) and archival multi-epoch imaging observations taken by *Spitzer/IRAC*. In addition, we present JHK_s photometry and near-IR spectroscopy of IC 10 X-2 taken at Palomar Observatory in 2016 July. We compare the near-IR spectroscopic features and the mid-IR color/magnitude of X-2 against various classes of supergiant stars to classify the stellar counterpart. We then study the optical light curve and consider possible accretion scenarios that result in SFXT flares.

2. OBSERVATIONS AND DATA REDUCTION

The primary source of our near-IR data was the Infrared Array Camera (IRAC) onboard the *Spitzer* Space Telescope. In its cold phase, IRAC imaged in four channels denoted by their wavelengths in microns ([3.6], [4.5], [5.8], and [8.0]). On 2009 May 15, IRAC transitioned to its warm phase, imaging only in channels [3.6] and [4.5]. X-2 was observed once during the cold phase and ten times during the warm phase.

X-2 was also imaged by the DUSTiNGS (Dust in Nearby Galaxies with Spitzer) program, a sample of 50 dwarf galaxies within 1.5 Mpc mapped with IRAC channels [3.6] and [4.5] (Boyer et al. 2015).

In addition, we performed near-IR imaging in the JHK_s channels and near-IR spectroscopy at Palomar Observatory on 2016 Jul 18. All IR fluxes are listed in Table 1.

2.1. *Spitzer photometry*

We demonstrate mid-IR variability concurrent with the 2010 X-ray outburst by constructing a light curve using archival *Spitzer* IRAC images. The flux density was calculated using a circle with 2.5" radius centered at X-2. Background flux density was calculated from an annulus centered at IC 10 X-2 with 3.5" inner radius and 6" outer radius to avoid contamination from nearby bright sources. The raw data (counts) were photometrically calibrated using IRAC specifications from Cutri et al. (2008), giving fluxes in mJy. The 1-σ uncertainty in the counts and fluxes were calculated by multiplying the uncertainty in the mean counts of the background annulus by the area of the 3" circle.

2.2. *P200 Near-IR Imaging and Spectroscopy*

To complement the *Spitzer* images, we obtained near-infrared images of IC 10-X2 in the J, H, and K_s bands on 2016 July 18 using the Wide Field Infrared Camera (WIRC; Wilson et al. 2003) on the 200-in. Hale Telescope at Palomar Observatory (P200). To allow accurate subtraction of the sky background, we took well-dithered sequences of 18 exposures of 60 s integration in J, 19 exposures of 25 s integration with 2 coadds in H, and 22 exposures of 15 s integration with 2 coadds in K_s, for total integration times of 1080 s in J, 950 s in H, and 660 s in K_s. Imaging reductions, including flat-fielding, background subtraction, astrometric alignment, and stacking of individual frames were performed using a custom pipeline. The photometric zero points of the final images were measured using aperture photometry of 7 isolated 2MASS stars in the field. Flux density was calculated using a circle with 3" radius centered at IC 10 X-2. Background flux density was calculated from an annulus centered at IC X-2 with 5" inner radius and 10" outer radius. Fluxes were converted to magnitudes assuming a Gaussian distribution of combined uncertainties from the 2MASS star zero-points and the X-2 photometry.

Near-infrared spectroscopy was performed using the Triple Spectrograph (TripleSpec) instrument during the same observation run to complement visible-spectrum spectroscopy by Laycock et al. (2014). We observed IC 10-X2 on 2017 July 8 with the near-IR Triple Spectrograph (TripleSpec) on the 200-in. Hale Telescope at Palomar Observatory. TripleSpec uses a 30×1 arcsec slit to obtain a JHK spectrum from 1–2.4 μm with a resolving power of 2500–2700. We obtained a sequence of 8 300 s exposures, for a total integration time of 2400 s. TripleSpec data were reduced using standard procedures with bias and flat field corrections. Wavelengths were calibrated against atmospheric lines.

2.3. *iPTF g- and R-band Photometry*

We used optical photometry of IC 10 X-2 from the IPAC/iPTF Discovery Engine (or IDE), which is described by Masci et al. (2017). Raw images from the Palomar 48-inch Samuel Oschin Schmidt Telescope and are run through a real-time pipeline, which performs basic calibration, then sent to PTFIDE, the image-differencing and transient extraction module. The images are returned to the pipeline for archiving, database-loading, and machine-learned vetting. The overall prod-

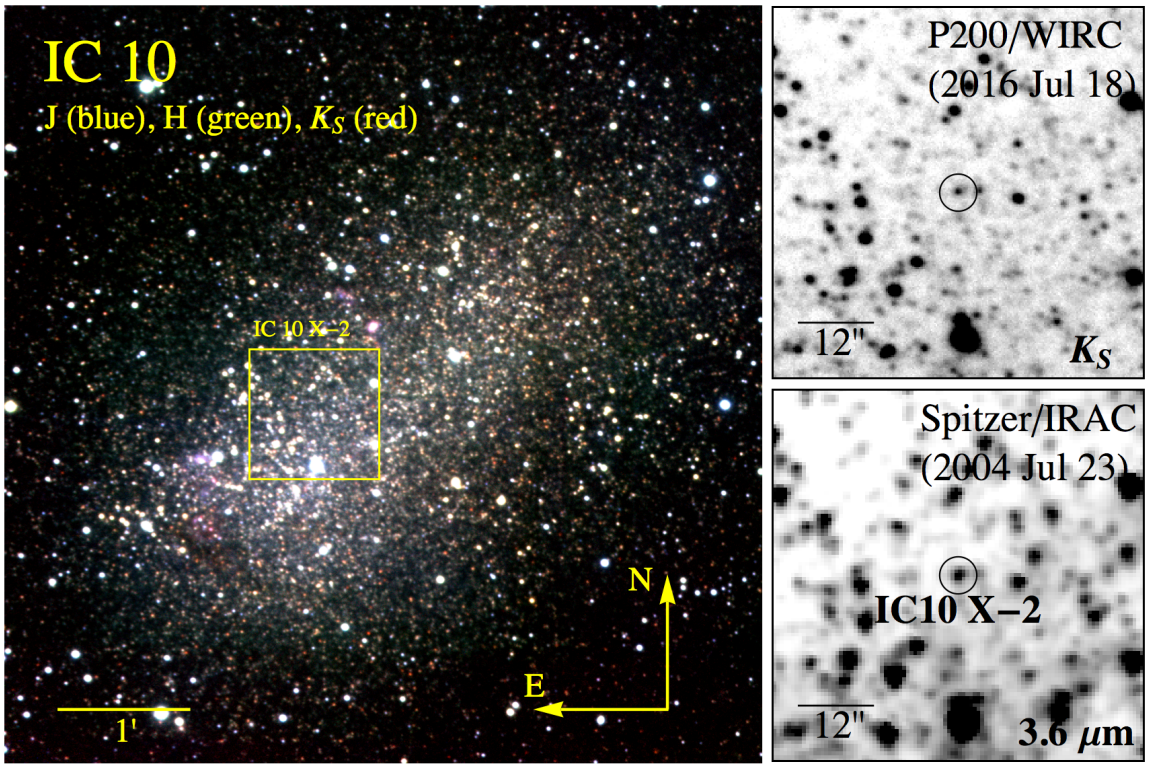


Figure 1. False color image of IC 10 taken with J (blue), H (green), and K_S (red) band filters by P200/WIRC on 2016 July 18. The 1 × 1' yellow box overlaid on the image is centered on IC 10 X-2 and corresponds to the field of view of the P200/WIRC K_S and *Spitzer*/IRAC Ch1 images shown on the right. The black circle overlaid on the images in the right is centered on the near- and mid-IR counterparts of IC 10 X-2 and represents the 3"-radius aperture used to perform the photometry.

ucts of the iPTF pipeline and PTFIDE are difference images, mask and uncertainty images, and QA metrics, in addition to candidate transient catalogs with PSF-fit and aperture photometry, and thumbnail images of transient candidates. Optical light curves in the R and g bands, spanning 2010 Nov 14 to 2017 Feb 14 and 2009 Aug 25 to 2017 Jan 10 respectively, were generated for IC 10 X-2.

3. RESULTS AND ANALYSIS

3.1. *IR and Optical Light Curves of IC 10 X-2*

An IR light curve of IC 10 X-2 is shown in Fig. 2. Between the initial mid-IR observations taken 2004 July 23 and more recent observations taken from 2010 - 2016, the [3.6] and [4.5] flux densities from X-2 decrease factors of 0.3 ($\sim 2\sigma$) and 0.35 ($\sim 4\sigma$), respectively. Four months prior to the 2010 May X-ray outburst, $\lesssim$month-timescale variability is detected between 2010 Jan 29 and 2010 Feb 19 where the [3.6] and [4.5] fluxes decreased by factors of 0.30 and 0.35, respectively.

Serendipitously, the three mid-IR observations preceding the outburst by $\sim 2-4$ months were taken within $\sim$weeks - months of *Chandra*/ACIS-S non-detections on 2010 Feb 11 and Apr 4 (Laycock et al. 2014). After the X-ray outburst, there is no obvious evidence of variability in the mid-IR with observations over the following ~ 6 yr. Post-outburst, the [3.6] and [4.5] fluxes exhibit approximately constant values of 0.20 and 0.15 Jy, respectively.

Both the optical R- and g-band light curves of X-2 exhibit high amplitude, short-duration flares that deviate significantly ($> 5\sigma$) from the quiescent brightness levels (Fig. 2). The median, "quiescent" magnitudes in the R and g bands were 18.64 ± 0.05 and 20.17 ± 0.08 Vega mag, respectively. A Lomb-Scargle periodogram analysis of the R-band light curve provided no significant periodicity in the variability.

A flare was defined to be a brightening event with an amplitude greater than 5σ above the quiescent magnitude. The brightest observed flare in the R-band occurred on 2013 Oct 10 (MJD 56575) and exhibited an amplitude of 1.32 mag. There were two detections of the 2013 Oct 10 flare taken 0.15 d apart, which provides a lower limit on the flare duration. Notably, this is the longest observed flare duration measured in the optical light curves. Upper limits were placed on the duration of each flare by defining the start and end of each flare to be magnitudes within or below 1σ of the quiescent

Table 1. IC 10 X-2 IR fluxes

MJD	UT start time	Filter (s)	Fluxes[a] (mJy)	Inst. or Database
2000-09-16	51803	JHK_s	0.419 ± 0.06, 0.708*, 0.421*	2MASS
2004-07-23	53209	[3.6], [4.5], [5.8], [8.0]	0.335 ± 0.02, 0.282 ± 0.01, 0.21 ± 0.04, 0.20 ± 0.03	IRAC
2010-01-29	55225	[3.6], [4.5]	0.236 ± 0.02, 0.184 ± 0.01	IRAC
2010-02-19	55246	[3.6], [4.5]	0.196 ± 0.02, 0.141 ± 0.01	IRAC
2010-03-10	55265	[3.6], [4.5]	0.234 ± 0.02, 0.152 ± 0.01	IRAC
2010-09-09	55448	[3.6], [4.5]	0.216 ± 0.02, 0.159 ± 0.01	IRAC
2010-10-04	55473	[3.6], [4.5]	0.223 ± 0.02, 0.164 ± 0.01	IRAC
2010-10-14	55483	[3.6], [4.5]	0.198 ± 0.02, 0.146 ± 0.01	IRAC
2011-09-24	55828	[3.6], [4.5]	0.199 ± 0.02, 0.150 ± 0.01	IRAC (DUSTiNGS[b])
2012-04-04	56021	[3.6], [4.5]	0.214 ± 0.02, 0.152 ± 0.01	IRAC (DUSTiNGS[b])
2015-03-11	57092	[3.6], [4.5]	0.184 ± 0.02, 0.138 ± 0.01	IRAC (DUSTiNGs[c])
2016-03-23	57470	[3.6], [4.5]	0.199 ± 0.02, 0.145 ± 0.01	IRAC (DUSTiNGs[c])
2016-07-18	57587	JHK_s	0.382 ± 0.06, 0.346 ± 0.03, 0.396 ± 0.08	WIRC[d]

[a] * denotes upper limits.

[b] PID 80063, Goldman et al. (in prep).

[c] PID 11041, Goldman et al. (in prep).

[d] The WIRC instrument was dithered at five positions in three quadrants (avoiding a quadrant with bad pixels).

brightness. The average upper limit determined for each flare is 8.0 d.

An average timescale between flare events of 15.1±7.8 d is derived for the R-band light curve of X-2. The > 60 d gaps in the light curve with no coverage of X-2 were omitted from this calculation. Interestingly, there were no flares observed at R- nor g-Band between 2015 Aug 5 (MJD 57239.4) and the end of the observations on 2017 Feb 14 (MJD 57798.1)

Short-duration and significant dips in brightness ($> 5\sigma$) are also apparent in both R- and g-band light curve in light curves of X-2. Only the dip on 2014 Jul 24 (MJD 56862.3) was detected with multiple consecutive observations, which provides a lower limit on the dip duration of 0.10 d. The highest amplitude dip was observed on 2015 Jan 25 (MJD 57047.2) and decreased to 0.62 mag below the quiescent brightness.

3.2. *Near-IR Spectroscopy*

The TripleSpec instrument detected near-IR continuum emission from X-2 and three emission lines with high signal-to-noise ratio (see Fig. 3). We identified them as Helium I (He I, 1.0819 μm), Paschen-Gamma (Pa γ, 1.0926 μm), and Paschen-Beta (Pa β, 1.2805 μm). Comparing to their rest frame wavelengths at 1.0830 μm, 1.0933 μm, and 1.2815 μm gives blueshifts of −314 km s^{-1}, −332 km s^{-1}, and −307 km s^{-1}, which are consistent with the −340 km s^{-1} for IC 10 (Laycock et al. 2014).

The center wavelengths and full-widths at half maximum (FWHM) were determined from Gaussian fits in CurveFit*Mathematica*[1], a *Mathematica* package. The FWHM were corrected for instrument resolution according to the equation:

$$FWHM_{corrected} = \sqrt{FWHM_{obs}^2 - FWHM_{instr}^2} \quad (1)$$

using the average spectral resolution 2600, from the 2500 − 2700 spectral resolution provided in TripleSpec instrument documentation.

The Pa γ and Pa β emission lines exhibit velocity widths near the 120 km s^{-1} spectral resolution of TripleSpec. The velocity width of the He I 10830 Å emission line, which provides a valuable diagnostic on the physical properties of stellar winds from massive stars (e.g. Groh et al. 2007 is $\sim$ 230 km s^{-1}. This velocity is consistent with winds from quiescent LBVs (Smith 2014; Humphreys et al. 2017) and the dense equatorial outflows from sgB[e] stars (de Wit et al. 2014) but slower than the $\gtrsim$ 1000 km s^{-1} outflows exhibited by OB supergiants and WR stars.

[1] http://www.sophphx.caltech.edu/CurveFit/

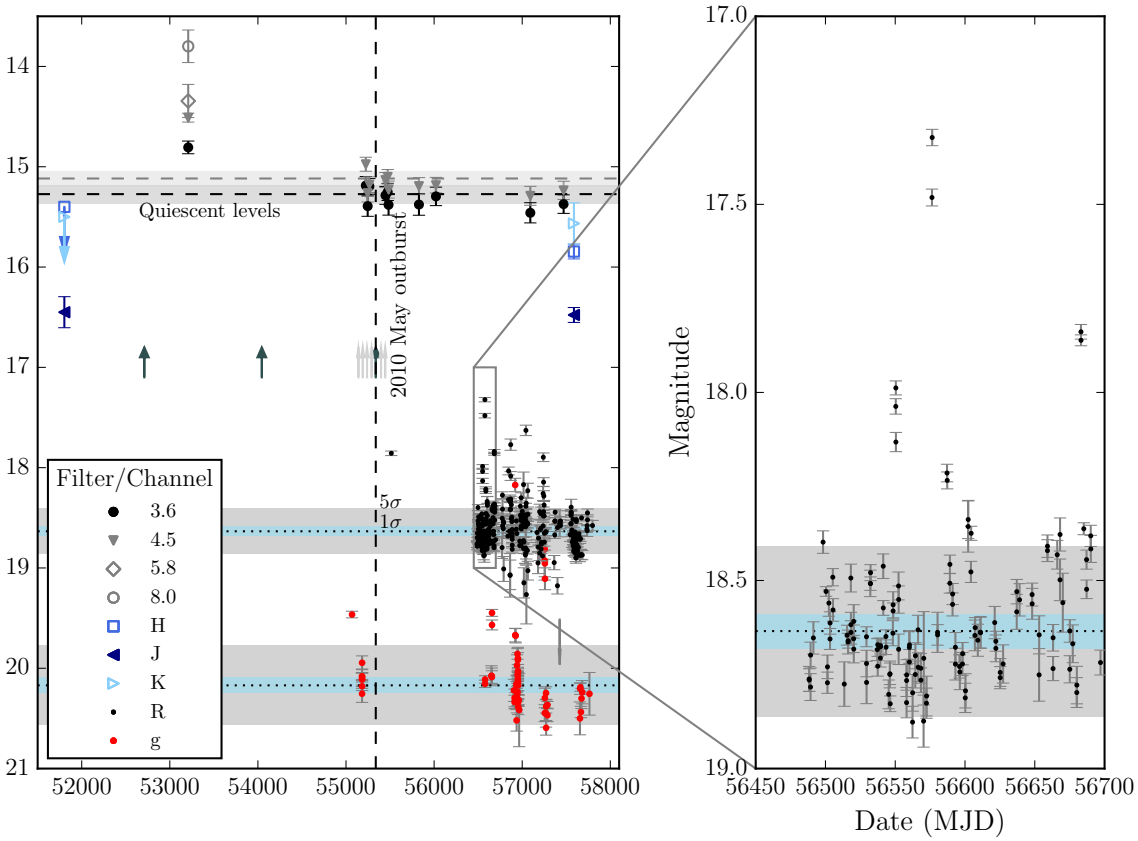


Figure 2. IC 10 X-2 near-IR and optical light curve, constructed from 11 *Spitzer* epochs (spanning 2004 Jul 23/52309 MJD to 2016 Mar 23/57470 MJD), 1 WIRC epoch, and optical data from iPTF. The [3.6] and [4.6] flux densities (mJy) drop by factors of 0.30 ($\sim 2\sigma$) and 0.35 ($\sim 4\sigma$) respectively shortly before the 2010 May X-ray outburst (dashed line, 55337 MJD). The quiescent levels for [3.6] and [4.5] were calculated as a simple average of the four most recent fluxes.
The arrows on the first set of H and K_s indicate that those fluxes are upper limits from the 2MASS database (size of errors unknown). The upward-pointing dark grey arrows indicate the X-ray detection epochs from Laycock et al. (2014); the upward-pointing light gray arrows indicate non-detections.
In the optical bands, the median magnitude is plotted, with 1 σ and 5 σ levels denoted.
Inset: A close-up of a densely sampled R-band light curve, showing several flares (defined to be $\geq 5\sigma$ detections).

4. DISCUSSION

4.1. *On the Nature of the IR Counterpart: an LBV Candidate*

In order to discern the nature of X-2's stellar counterpart, we compare its near-IR spectum with the Groh et al. (2007) spectral atlas around He I 10830 Å encompassing four categories of stars: (1) Be type, (2) LBV/LBV candidates (LBVc)/ex- or dormant LBVs, (3) OB supergiants, and (4) Wolf-Rayets. The $\sim$ 230 km s^{-1} width of X-2's He I peak rules out the Wolf-Rayet class, which exhibits a broad ($\gtrsim$ 1000 km s^{-1}) He I emission line. Additionally, Wolf-Rayet stars are typically Hydrogen-poor which contradicts the clear presence of Hydrogen in X-2. X-2 has equally strong He I and Pa γ lines, ruling out OB supergiants, in which the former is much stronger than the latter. In the remaining two categories, X-2 most resembles the LBVc W243 (Clark & Negueruela 2004) and the classical Be star HD 120991 that exhibit He I and Pa γ lines of similar amplitude and width. It should be noted that LBVs exhibit spectroscopic variability, altering the relative strengths of the lines.

Another means of classifying the IR counterpart of IC 10 X-2 came from plotting its [3.6] color vs. [3.6] - [4.5] magnitude on a color-magnitude diagram (CMD) of known supergiant stars in the Large Magellanic Cloud (LMC) with *Spitzer* counterparts shown in Fig. 4 of Bonanos et al. (2009). The original color-magnitude diagram was recreated from online data published by Bonanos et al. (2009). We used $\mu = 18.91$ for the LMC distance modulus (Bonanos et al. 2009), and $\mu = 24.1$ for the galaxy IC 10 (Laycock et al. 2014). Throughout the observed mid-IR evolution, X-2 occupies a region in the mid-IR CMD consistent with A-, F-, G-type supergiants (AFG/comp in Fig. 4), late and early B-type supergiants, Wolf Rayets, and LBVs. Notably, X-2 is over two magnitudes brighter at 3.6 μm than the Be-XRB,

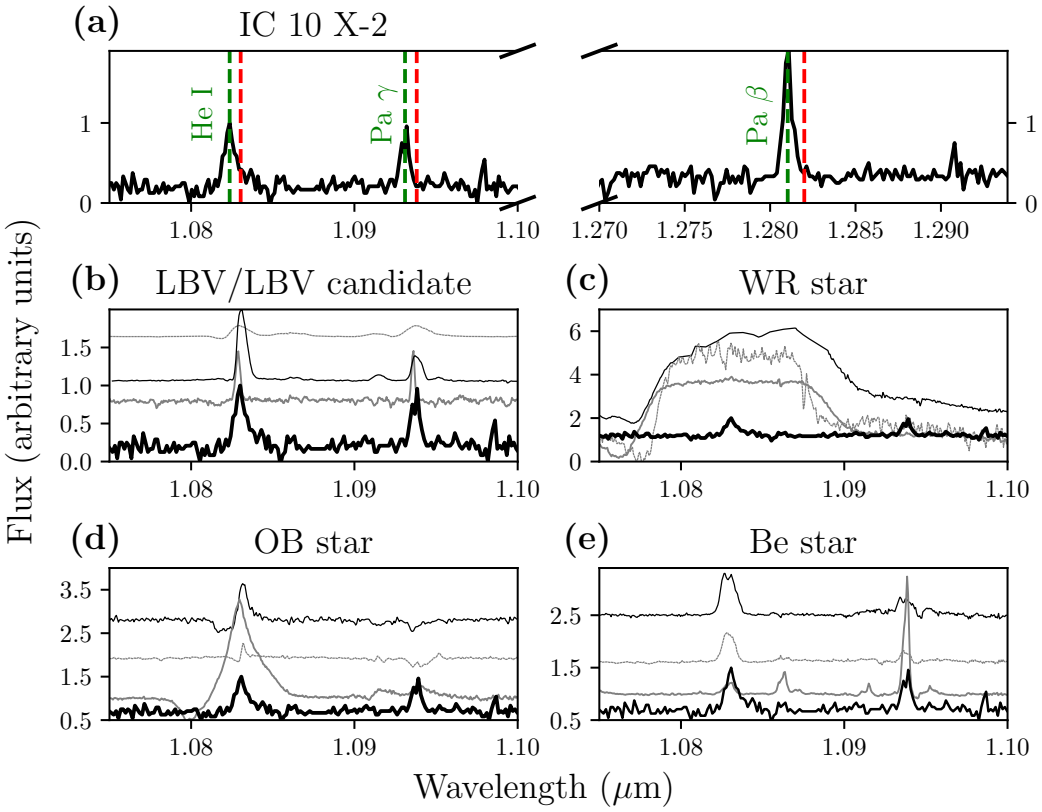


Figure 3. **(a)** He I, Paschen-Gamma (Pa γ), and Paschen-Beta (Pa β) emission lines detected with strong (>5) signal-to-noise ratio in the TripleSpec observations. The observed blueshifted and rest frame wavelengths for the three lines are indicated by the green and red dashed lines respectively. The latter two lines are close to the instrument resolution limit. The apparent double peak in the plot for Pa γ is most likely an artifact. **(b)-(e)** IC 10 X-2's rest-frame spectrum plotted with representative spectra of various stars from Groh et al. (2007). The other lines, denoted with solid black, dashed grey, and solid grey, correspond to the following stars. **(b)** LBVs: W243 A2 Ia, HD 316286, and AG Carinae. **(c)** Wolf-Rayet stars: WR 90 WC7, WR 136 WN6(h), WR6 WN4. **(d)** OB stars: HD 152408 O8 Iafpe, HD 80077 B2 Ia+, HD 169454 B1 Ia+. **(e)** Be stars: χ Oph B1.5Ve, δ Sco B0.31Ve, χ Per B0Ve.

which implies that the IR counterpart is unlikely a classical Be star. Wolf-Rayet and Early B-type supergiants are ruled out based on the properties of their near-IR emission lines discussed above. It is unlikely that X-2 is an AFG/late-B supergiant given the hardness of the radiation field required to produce the observed near-IR emission lines (Fig. 3) noting also the absence of these feature in early B supergiants. We therefore interpret X-2 as an LBV/LBVc, which is supported by the presence of characteristic optical emission lines revealed by Laycock et al. (2014) (e.g. He II 4686).

LBVs typically exhibit luminosities greater than a few times 10^5 $L_\odot$ (Smith 2014). It is difficult to determine the bolometric luminosity of X-2 due to uncertainties in the line of sight extinction; however, Laycock et al. (2014) estimate extinction-corrected V-band magnitudes of X-2 as $M_V = -6.78$ for optically derived de-reddening and $M_V = -7.51$ for X-ray derived de-reddening. Assuming a bolometric correction of -1.68 mag, the approximate value for the LBV AG Carinae in 2002 March-July (Groh et al. 2009a), we estimate the luminosity of X-2 to be $\sim 2-4\times10^5$ $L_\odot$. This range of luminosities is consistent with the values exhibited by lower luminosity LBVs. We note that although the bolometric corrections will depend on the effective temperature of the star, there are LBVs that have absolute visual magnitudes consistent with X-2 ($M_V \sim -7$; Humphreys et al. 2014).

4.2. *Mid-IR Free-Free Emission from Ionized Winds*

Massive stars with strong winds such as LBV and Wolf-Rayet stars can exhibit an IR excess due to free-free emission from their outflows (e.g. Cohen et al. 1975). However, an IR excess may also be attributed to the presence of warm circumstellar dust. We attempt to distinguish the nature of the mid-IR emission by performing a power-law fit, $F_\nu = C\,\lambda^\alpha$ mJy, to the 3.6, 4.5, 5.8 and 8.0 μm photometry taken 2004 Jul 23. The best-fit provides $C = 0.9 \pm 0.2$ mJy and $\alpha = -0.76 \pm 0.12$. This slope is consistent with the predicted $\alpha \sim -0.6$

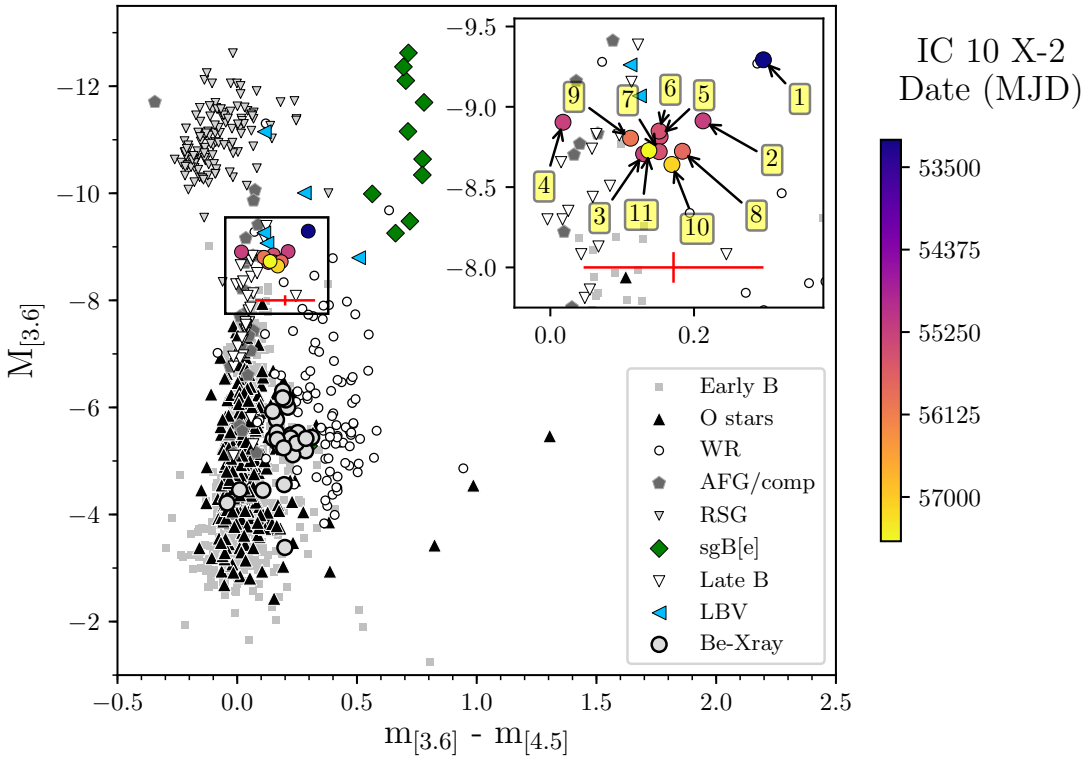


Figure 4. [3.6] - [4.5] color vs. [3.6] absolute magnitude of massive stars with IRAC counterparts in the Large Magellanic Cloud from Figure 2 of Bonanos et al. (2009). IC 10 X-2 is plotted over eleven epochs spanning 2004 to 2016 (see color bar and inset). The error bar for the color and absolute magnitude of X-2 was calculated from uncertainties in the flux. The IC 10 distance modulus was taken to be 24.1 (Laycock et al. 2014).

value for free-free emission from an ionized outflow from a star with a spherical expansion and constant velocity (e.g. Wright & Barlow 1975). The source of the mid-IR emission is unlikely due to dust given that color temperature estimates for the mid-IR emission at 3.6 and 4.5 μm indicate values of $\sim$ 1700 K, which is hotter than dust sublimation temperatures ($\sim$ 1200 K; Draine 2011). We therefore interpret the IR excess from X-2 as free-free emission.

Work by Humphreys et al. (2017) on distinguishing LBVs/LBVcs and supergiant B[e] stars shows that the IR spectral energy distribution from LBVs exhibit free-free emission with no evidence for warm circumstellar dust. Most supergiant B[e] stars however, are found to have warm circumstellar dust. Humphreys et al. (2017) also indicate that dusty/non-dusty LBV/sgB[e] stars are clearly separated in mid-IR color space, where stars with $[3.6] - [4.5] < 0.5$ do not show warm circumstellar dust. This distinction between sgB[e] and LBV stars is also noticeable in Fig. 4 and supports the interpretation of X-2 as an LBV/LBVc.

If the mid-IR flux originates from free-free emission in the winds of IC 10 X-2's optical counterpart, the fluxes can be used to estimate its mass-loss rate (e.g. Fuchs et al. 2006). Adopting the formalism of Wright & Barlow (1975) and assuming a thick geometry for the wind (i.e. the ratio of structural size scales in the outflow do not exceed $\sim$ 10), the mass-loss rate, $\dot{M}_w$, is related to the mid-IR flux at 4.5 μm, $F_{4.5}$, and other outflow properties as follows:

$$\dot{M}_w \sim 6 \times 10^{-5} \frac{\mu}{\gamma_e^{1/2}\, g^{1/2}\, Z} \left(\frac{d}{660\,\mathrm{kpc}}\right)^{3/2} \cdot \left(\frac{F_{4.5}}{174\,\mu\mathrm{Jy}}\right)^{3/4} \left(\frac{v_w}{200\,\mathrm{km\,s^{-1}}}\right) \mathrm{M}\odot\ \mathrm{yr}^{-1}, \quad (2)$$

where $\mu = 1$ is the mean molecular weight per nucleon, d is the distance to IC 10 X-2, v_w is the wind velocity, $\gamma_e = 1$ is the number of free electrons per nucleon, $g = 1$ is the Gaunt factor, $Z = 1$ is the mean charge per ion. The mass-loss rates determined by Eq. 2 from the range of fluxes exhibited by IC 10 X-2 at 4.5 μm is $\dot{M}_w \approx 3 \times 10^{-5} - 10^{-4}$ M$_\odot$ yr^{-1} , which is consistent with the mass-loss rates exhibited by LBVs in quiescence (e.g. Smith 2014).

4.3. *Interpreting the Optical and X-Ray Outbursts*

Since the optical and X-ray data were not acquired contemporaneously, it is difficult to determine whether or not the X-ray and optical variability share the same origin. However, the $\sim$ 0.15 d ($\sim$ 4 hr) lower-limit on the optical variability timescale is consistent with observed durations of X-ray flares from known SFXTs (a few hours; Romano et al. 2014).

We can address whether the short timescale (0.15 d $\lesssim \Delta t \lesssim$ 4 d) and high amplitude ($\sim$ 1 mag) variability exhibited by X-2 (Fig. 2) is due to activity from the stellar counterpart or linked to the binary nature of the system. LBVs and OB supergiants are known to exhibit optical variability on similarly short timescales of days to weeks, but the brightness only varies by up to a few tenths of a magnitude (e.g. Bresolin et al. 2004). Alternatively, LBVs are known to undergo phases of extreme photometric variability from 1 - 2 mag but on timescales of years to decades. The short timescale, high amplitude variability from X-2 is therefore most likely due to the presence of the compact object and linked to the X-ray variability.

There are several mechanisms considered for SFXTs that could account for the short optical flares from X-2. The flares may be due to accretion of clumpy winds from the donor star, motion of the compact object through an asymmetric outflow, and/or "gated" accretion due to magnetic processes (see Sidoli 2013 and ref. therein). With the available data on X-2, it is difficult to address the later mechanism; however, we can study the first two in the theoretical framework of Bondi-Hoyle accretion (e.g. Davidson & Ostriker 1973).

Assuming an accreting compact object of mass M_{CO} is traveling at a velocity v_{rel} relative to the winds from the supergiant donor star of mass M_* with a mass-loss rate $\dot{M}_w$ and outflow velocity v_w, the accretion rate onto the compact object can be approximated by

$$\dot{M}_{\rm acc} = \zeta \frac{(G\,M_{\rm CO})^2}{v_{\rm rel}^3} \frac{\dot{M}_{\rm w}}{a^2\,v_{\rm w}}, \qquad (3)$$

where a is the orbital separation between the compact object and donor star, and ζ is the correction factor for radiation pressure and the finite gas cooling time (assumed to be $\zeta = 1$, e.g. Oskinova, Feldmeier, & Kretschmar 2012). The relative velocity between the winds and the orbital motion of the compact object moving at a speed of v_{CO} is

$$v_{rel} = \sqrt{v_{CO}^2 + v_w^2}, \qquad (4)$$

where v_{CO} can be approximated by $v_{CO} \approx \sqrt{GM_*/a}$ assuming nearly circular orbits and $M_* >> M_{\rm CO}$. The X-ray luminosity from the accreting compact object is then

$$L_X = \eta\,\dot{M}_{acc}c^2 \approx \eta\,\zeta \frac{(G\,M_{\rm CO})^2}{(\frac{GM_*}{a} + v_w^2)^{3/2}} \frac{\dot{M}_{\rm w}}{a^2\,v_{\rm w}} c^2, \qquad (5)$$

where η is an efficiency factor that depends on the accretion physics and is assumed to be $\eta \sim 0.1$ (e.g. Oskinova, Feldmeier, & Kretschmar 2012).

In order to test the viability of Eq. 5, we use it to compare against the orbital period ($P_{\rm orb}$ = 8.95 d) of the well-studied wind-fed HMXB Vela X-1 (Hiltner et al. 1972; Lamers et al. 1976; Quaintrell et al. 2003). We adopt the Vela X-1 supergiant stellar wind velocity, mass, and mass-loss rate provided by Giménez-García et al. (2016) and the X-ray luminosity derived by Sako et al. (1999): $v_w = 264$ km s^{-1} $M_* = 21.5$ M$_\odot$, $\dot{M} = 6.3 \times 10^{-7}$ M$_\odot$ yr^{-1}, and L$_X = 4.5 \times 10^{36}$ erg s^{-1}. Assuming the mass of the accreting neutron star is $M_{\rm CO} = 1.5$ M$_\odot$, we estimate from Eq. 5 and Kepler's 3rd Law that $P_{\rm orb} \sim$ 16 d, which is within a factor of 2 of the observed orbital period for Vela X-1. Equation 5 should therefore provide reasonable estimates or limits for the orbital parameters of wind-fed X-ray binaries in nearly circular orbits.

First, we consider the scenario where the optical/X-ray flares were due to the compact object encountering an asymmetric outflow from the stellar counterpart. Such mass-loss asymmetries are naturally inferred for stars that are observed to be rapidly rotating like bonafide galactic LBVs (e.g. Groh et al. 2009b). Adopting the derived mass-loss rate of $\dot{M}_w \sim 5 \times 10^{-5}$ M$_\odot$ yr^{-1} and wind velocity v$_w \sim$ 200 km s^{-1}, and assuming a donor star mass of $M_* \sim 30$ M$_\odot$ and compact object mass of M$_{CO} \sim 1.5$ M$_\odot$, we find from Eq. 5 and Kepler's 3rd Law that for the range of X-ray luminosities exhibited by X-2 in outburst, $L_X = 3.4\times10^{36} - 1.8\times10^{37}$ erg s^{-1},

$$P_{orb} \sim 500 - 8600 \text{ d}. \qquad (6)$$

The derived orbital timescales under the asymmetric outflow scenario are over an order of magnitude longer than the observed timescales between optical flares ($\sim$ 15 d; Sec. 3.1). The timing of the flares in this scenario should also be periodic since they correspond to the orbital motion of the compact object through the stellar outflow. The lack of any significant periodicities identified in a Lomb-Scargle periodogram analysis of the X-2 optical light and the inconsistency between the theoretical and observed flare timescales suggests that the SFXT flares from X-2 did not originate from interactions between the compact object and an asymmetric outflow.

We now consider the scenario were the optical/X-ray flares from X-2 were due to accretion of clumps in

an inhomogeneous outflow from the stellar counterpart. Clumping in the winds of massive stars has been observationally confirmed and is also backed by stellar wind theory (e.g. Oskinova, Feldmeier, & Kretschmar 2012). With the observational constraints on the flare duration, $\Delta t \sim 0.2 - 8$ d, and the time between flares, $T \sim 15$ d, the clump volume filling factor, f_V, can be estimated for the stellar outflow of X-2 and compared with the f_V of supergiant winds.

Assuming a simple model where the outflows consist entirely of clumps with radius R_{cl} and mass M_{cl}, the clump volume filling factor is given by the ratio of the homogeneous wind density, ρ_h, and the individual clump density, ρ_{cl}: $f_V = \frac{\rho_h}{\rho_{cl}}$. The homogeneous wind and clump densities can be written as

$$\rho_h = \frac{\dot{M}_{cl}}{4\pi\, R^2\, v_{cl}} \text{ and } \rho_{cl} = \frac{M_{cl}}{4/3\,\pi\, R_{cl}^3}, \tag{7}$$

respectively, where $\dot{M}_{cl}$ is mass-loss from the clumped outflow, R is the distance between the stellar counterpart and compact object, and v_{cl} is the clump outflow velocity. $\dot{M}_{cl}$ can be related to the timescale between the flares, T, as follows (see Walter & Zurita Heras 2007):

$$\dot{M}_{cl} = \frac{4\, R^2 M_{cl}}{R_{cl}^2\, T}. \tag{8}$$

By combining Eq. 7 and 8, f_V can then be expressed as

$$f_V = \frac{4\, R_{cl}}{3\, T\, v_{cl}} \sim \frac{4\, \Delta t}{3\, T}, \tag{9}$$

where we assumed $R_{cl} \sim v_{cl}\, \Delta t$. Given the observed constraints for X-2 on $\Delta t \sim 0.2 - 8$ d and $T \sim 15$ d, we determine from Eq. 9 that

$$0.01 < f_V < 0.71. \tag{10}$$

Although the upper limit of f_v is not well constrained from our observations, the range of values for f_V overlaps with observationally derived clump volume filling factors for massive star winds: $f_V \sim 0.02 - 0.1$ (e.g. Bouret, Lanz, & Hillier 2005; Oskinova, Hamann, & Feldmeier 2007). The additional evidence of "eclipses" in the light curve, which may arise from optically thick clumps in the winds of the optical counterpart (Fig. 2), supports the interpretation of the optical flares as clump accretion onto the compact object.

5. CONCLUSION

We report time-varying characteristics of the optical and IR counterpart to IC 10 X-2, a supergiant fast X-ray transient candidate discovered by its X-ray outbursts in 2004 and 2010 (Laycock et al. 2014). We utilize observations taken by *Spitzer* in the mid-IR, WIRC and TripleSpec in the near-IR, and iPTF at optical bands. Although there are no concurrent observations with the X-ray transient events from X-2, the optical and IR data provide valuable information on the nature of the stellar counterpart and its outflow that may be contributing to the X-ray flares.

Near-IR spectroscopy of X-2 reveal moderately resolved ($\sim$ 200 km s^{-1}) hydrogen and helium emission lines that rule out stellar counterparts that exhibit high wind velocities like OB supergiants and WR stars. The presence of these lines also rules out the stars that exhibit low ionizing fluxes like A, F, G, or late B supergiants. The spectra more closely resemble the properties of an LBV/LBVc. This LBV/LBVc interpretation is supported by the similar mid-IR color and magnitude X-2 shares with LBVs observed in the LMC (Fig. 1) and the 6×10^{-5} M$_\odot$ yr^{-1} mass-loss rate estimated from the mid-IR flux assuming it originates from free-free emission in ionized winds. This mass-loss rate is consistent with LBVs in quiescence.

The second key result from our analysis is the presence of short ($\sim$ day) high amplitude ($\sim$ 1 mag) optical flares and eclipses in the iPTF light curves taken between 2009 and 2017. We interpret the origin of the flares as accretion of optically thick clumps formed in the winds of the stellar companion in X-2 on to the compact object. Constraints on the clump volume filling factor in the stellar winds as determined by the timing and duration of the optical flares show a range of values that overlap with the observed clump volume filling factor in massive star winds.

Currently, only 12 SFXTs (Romano et al. 2014) and $\sim$ 20 bona-fide LBVs are known. X-2, as an SFXT candidate hosting an LBV/LBVc, is therefore at the cross section of these two rare classes of sources. Future coordinated, multi-wavelength observations of X-2 present a unique opportunity to study the accretion processes in SFTXs and the interactions between the compact object and the mass-loss from an LBV/LBVc companion.

This project received funding from the California Institute of Technology Student-Faculty Program's Summer Undergraduate Research Fellowship (SURF) and the Flintridge Foundation. S. Kwan would like to thank M. Kasliwal, R. Lau, and J. Jencson for their mentorship. R. Lau thanks M. Heida for the valuable discussion on SFXTs. We thank the *Spitzer* InfraRed Intensive Transient Survey team and Palomar Observatory for their scientific support. Palomar Observatory is owned and operated by the California Institute of Technology, and administered by Caltech Optical Observatories.

This publication makes use of data products from the Two Micron All Sky Survey, which is a joint project of the University of Massachusetts and the Infrared

Processing and Analysis Center/California Institute of Technology, funded by the National Aeronautics and Space Administration and the National Science Foundation.

This research has made use of the SVO Filter Profile Service (http://svo2.cab.inta-csic.es/theory/fps/) supported from the Spanish MINECO through grant AyA2014-55216.

Facilities: P200(WIRC, TripleSpec), Spitzer IRAC

Software: SAO DS9, Python, Mathematica

Table 2. R-band Photometry

Date(MJD)	Mag
55514.23616	17.86 ± 0.02
56488.32939	18.76 ± 0.03
56488.36582	18.76 ± 0.03
56489.32626	18.78 ± 0.04
56489.36289	18.70 ± 0.03
56491.35721	18.65 ± 0.04
56498.2898	18.40 ± 0.03
56500.43422	18.53 ± 0.01
56501.41988	18.77 ± 0.03
56501.45605	18.73 ± 0.03
56502.46742	18.56 ± 0.04
56503.27465	18.66 ± 0.03
56503.31132	18.61 ± 0.03
56505.27163	18.49 ± 0.02
56505.41425	18.58 ± 0.03
56513.5047	18.78 ± 0.06
56515.4967	18.65 ± 0.03
56516.20826	18.66 ± 0.03
56516.24802	18.66 ± 0.02
56518.20242	18.49 ± 0.04
56518.25131	18.62 ± 0.03
56518.29041	18.64 ± 0.03
56520.19334	18.65 ± 0.04
56520.25701	18.61 ± 0.04
56520.29488	18.68 ± 0.04
56529.39718	18.65 ± 0.03
56529.43346	18.72 ± 0.04
56529.4695	18.77 ± 0.06
56532.1597	18.51 ± 0.04
56532.24578	18.51 ± 0.02
56532.31912	18.48 ± 0.02
56537.16429	18.68 ± 0.03
56537.45612	18.73 ± 0.03
56537.4925	18.67 ± 0.02
56539.39483	18.71 ± 0.02
56539.43118	18.67 ± 0.02
56539.46814	18.68 ± 0.02
56541.40691	18.46 ± 0.03
56541.44414	18.57 ± 0.02
56543.34669	18.65 ± 0.02
56543.43679	18.68 ± 0.02

Table 2 continued

Table 2 *(continued)*

Date(MJD)	Mag
56545.33896	18.80 ± 0.04
56546.14125	18.75 ± 0.04
56546.24068	18.75 ± 0.03
56546.41507	18.83 ± 0.02
56548.318	18.64 ± 0.03
56548.45631	18.58 ± 0.02
56548.49296	18.56 ± 0.03
56550.40024	18.04 ± 0.02
56550.44832	17.99 ± 0.02
56550.48191	18.13 ± 0.03
56552.38512	18.51 ± 0.04
56552.4323	18.68 ± 0.04
56552.46575	18.55 ± 0.04
56558.12679	18.82 ± 0.04
56558.1594	18.77 ± 0.04
56558.19295	18.75 ± 0.04
56560.11681	18.68 ± 0.04
56560.15059	18.72 ± 0.03
56560.20559	18.67 ± 0.04
56562.40247	18.88 ± 0.04
56562.47419	18.80 ± 0.05
56564.38602	18.75 ± 0.04
56564.46833	18.70 ± 0.03
56566.37091	18.63 ± 0.04
56566.44337	18.73 ± 0.04
56568.34645	18.73 ± 0.04
56568.41987	18.76 ± 0.03
56570.32339	18.87 ± 0.07
56570.46095	18.71 ± 0.12
56572.36285	18.83 ± 0.04
56572.44725	18.81 ± 0.05
56576.33208	17.48 ± 0.02
56576.48402	17.32 ± 0.02
56580.32748	18.64 ± 0.05
56580.35282	18.64 ± 0.03
56587.12142	18.21 ± 0.02
56587.25208	18.23 ± 0.02
56589.15391	18.51 ± 0.03
56589.18001	18.46 ± 0.02
56591.09043	18.56 ± 0.03
56591.11758	18.54 ± 0.03
56593.10497	18.68 ± 0.04
56593.13542	18.72 ± 0.04

Table 2 continued

Table 2 *(continued)*

Date(MJD)	Mag
56596.09009	18.73 ± 0.03
56596.29199	18.74 ± 0.05
56598.19435	18.72 ± 0.03
56598.27627	18.69 ± 0.03
56600.19255	18.81 ± 0.04
56600.35051	18.79 ± 0.05
56602.25343	18.36 ± 0.07
56602.27883	18.34 ± 0.05
56604.23115	18.48 ± 0.03
56604.40069	18.37 ± 0.02
56607.08198	18.65 ± 0.04
56607.28429	18.63 ± 0.03
56609.17745	18.66 ± 0.04
56611.10898	18.64 ± 0.04
56611.13329	18.64 ± 0.04
56621.29479	18.61 ± 0.04
56622.08446	18.66 ± 0.03
56622.10905	18.68 ± 0.04
56625.20354	18.76 ± 0.03
56625.23247	18.74 ± 0.04
56627.30289	18.72 ± 0.05
56637.08132	18.58 ± 0.05
56637.10642	18.53 ± 0.03
56639.10692	18.55 ± 0.04
56648.0828	18.54 ± 0.03
56648.10917	18.56 ± 0.04
56653.09568	18.75 ± 0.07
56653.13734	18.64 ± 0.05
56659.08707	18.42 ± 0.03
56659.1119	18.41 ± 0.03
56663.09284	18.73 ± 0.03
56663.11843	18.65 ± 0.04
56666.08588	18.43 ± 0.04
56668.0877	18.50 ± 0.06
56668.11222	18.38 ± 0.04
56670.08942	18.56 ± 0.08
56675.09919	18.74 ± 0.04
56675.14168	18.63 ± 0.03
56677.21062	18.67 ± 0.05
56680.10995	18.80 ± 0.04
56680.1374	18.78 ± 0.05
56683.09992	17.84 ± 0.02
56683.13194	17.86 ± 0.01

Table 2 continued

Table 2 *(continued)*

Date(MJD)	Mag
56685.1092	18.36 ± 0.02
56687.10219	18.44 ± 0.03
56687.14475	18.52 ± 0.02
56690.1052	18.38 ± 0.03
56690.15279	18.42 ± 0.04
56697.11039	18.72 ± 0.03
56771.50559	18.80 ± 0.11
56772.50256	18.51 ± 0.08
56775.49464	18.27 ± 0.03
56776.49197	18.41 ± 0.09
56777.48838	18.58 ± 0.12
56785.46738	18.61 ± 0.04
56785.49089	18.54 ± 0.06
56789.45628	19.01 ± 0.12
56789.48222	18.55 ± 0.06
56837.47402	18.68 ± 0.02
56845.45242	18.03 ± 0.04
56845.47884	18.32 ± 0.02
56855.46222	18.63 ± 0.04
56862.27785	19.07 ± 0.15
56862.3165	19.07 ± 0.22
56862.3553	18.42 ± 0.07
56862.38817	18.34 ± 0.07
56869.37086	18.42 ± 0.02
56869.40135	18.08 ± 0.04
56869.43428	18.33 ± 0.02
56869.46248	17.77 ± 0.06
56869.49927	18.31 ± 0.03
56876.41522	18.67 ± 0.02
56876.44466	18.63 ± 0.02
56876.45058	18.51 ± 0.03
56876.48899	18.37 ± 0.03
56882.38472	18.49 ± 0.02
56882.45426	18.54 ± 0.03
56886.40657	18.81 ± 0.03
56886.43473	18.66 ± 0.04
56886.46407	18.77 ± 0.03
56886.48626	18.62 ± 0.04
56886.49722	18.68 ± 0.03
56886.50936	18.71 ± 0.04
56932.49492	18.53 ± 0.04
56932.52231	18.61 ± 0.10
56940.10688	18.66 ± 0.07

Table 2 continued

Table 2 *(continued)*

Date(MJD)	Mag
56972.2089	18.73 ± 0.04
56972.23176	18.78 ± 0.05
56979.21826	18.38 ± 0.05
56980.21221	18.47 ± 0.03
56986.22259	18.60 ± 0.04
56986.28578	18.53 ± 0.05
56987.20258	18.78 ± 0.03
56987.26433	18.51 ± 0.13
56988.16044	18.30 ± 0.05
56989.10013	18.58 ± 0.04
56989.16557	18.61 ± 0.03
56990.09579	18.50 ± 0.08
56990.15965	18.52 ± 0.02
57000.12383	18.48 ± 0.05
57000.15459	18.53 ± 0.04
57001.10524	18.44 ± 0.03
57001.13257	18.50 ± 0.02
57011.12233	18.47 ± 0.03
57011.14887	18.55 ± 0.03
57014.10122	18.73 ± 0.04
57014.12328	18.56 ± 0.05
57015.09928	18.81 ± 0.05
57015.11895	18.17 ± 0.13
57018.10068	18.54 ± 0.04
57018.12509	18.58 ± 0.04
57019.09567	19.15 ± 0.15
57019.10936	18.74 ± 0.05
57030.09887	18.52 ± 0.04
57030.16275	18.55 ± 0.04
57036.11696	18.87 ± 0.08
57037.10262	18.49 ± 0.03
57037.15286	18.53 ± 0.04
57038.15338	18.80 ± 0.15
57039.10544	18.59 ± 0.03
57039.13707	18.55 ± 0.02
57040.10478	18.49 ± 0.03
57040.15436	18.85 ± 0.11
57041.14765	18.38 ± 0.03
57042.10102	18.47 ± 0.02
57042.1477	17.63 ± 0.05
57043.10185	18.55 ± 0.14
57043.14678	18.54 ± 0.03
57046.10066	18.35 ± 0.05

Table 2 continued

Table 2 *(continued)*

Date(MJD)	Mag
57046.14241	18.82 ± 0.09
57047.15525	19.27 ± 0.29
57059.10799	18.83 ± 0.04
57059.11758	18.55 ± 0.04
57063.10801	18.56 ± 0.04
57063.12001	18.23 ± 0.07
57064.1092	18.46 ± 0.07
57064.12826	19.03 ± 0.09
57168.46631	18.65 ± 0.07
57179.4764	18.95 ± 0.11
57180.45855	18.79 ± 0.04
57185.46873	18.70 ± 0.07
57198.43492	18.85 ± 0.08
57198.46803	18.44 ± 0.08
57207.48208	18.62 ± 0.03
57210.43863	18.61 ± 0.03
57210.47753	18.46 ± 0.07
57214.46127	18.81 ± 0.05
57218.42646	18.76 ± 0.03
57218.47632	18.75 ± 0.02
57230.4439	18.88 ± 0.05
57237.43162	18.58 ± 0.03
57237.48108	18.26 ± 0.07
57239.42503	17.90 ± 0.04
57239.47012	18.48 ± 0.05
57242.35853	18.44 ± 0.05
57242.40331	18.14 ± 0.04
57245.30272	18.48 ± 0.03
57245.33991	18.28 ± 0.05
57248.3374	18.37 ± 0.05
57248.37045	18.48 ± 0.02
57251.32752	18.65 ± 0.05
57251.35716	18.74 ± 0.04
57267.43427	18.65 ± 0.03
57267.47725	18.64 ± 0.04
57363.09105	18.95 ± 0.07
57369.08424	18.67 ± 0.04
57369.0931	18.53 ± 0.04
57374.08289	18.53 ± 0.03
57374.09191	18.44 ± 0.03
57400.09411	18.60 ± 0.04
57400.10291	19.18 ± 0.08
57425.1106	18.56 ± 0.13

Table 2 continued

Table 2 *(continued)*

Date(MJD)	Mag
57431.10759	18.53 ± 0.04
57431.11384	18.56 ± 0.04
57434.12007	18.53 ± 0.05
57434.12381	18.58 ± 0.03
57544.48028	18.67 ± 0.07
57552.47619	18.56 ± 0.03
57553.48097	18.48 ± 0.05
57554.4719	18.56 ± 0.03
57555.4413	18.46 ± 0.03
57555.4413	18.45 ± 0.03
57555.46503	18.39 ± 0.08
57555.46503	18.45 ± 0.02
57564.44525	18.62 ± 0.05
57564.45274	18.63 ± 0.05
57567.48385	18.74 ± 0.06
57577.4716	18.77 ± 0.04
57578.4553	18.73 ± 0.04
57578.4553	18.52 ± 0.04
57578.48498	18.67 ± 0.04
57578.48498	18.69 ± 0.04
57584.45806	18.70 ± 0.04
57585.44955	18.69 ± 0.10
57585.44955	18.83 ± 0.05
57585.48817	18.80 ± 0.05
57586.43409	18.76 ± 0.04
57586.47677	18.84 ± 0.04
57596.45579	18.69 ± 0.04
57596.4886	18.77 ± 0.05
57599.46419	18.78 ± 0.04
57600.48294	18.64 ± 0.03
57601.47029	18.76 ± 0.04
57602.47299	18.83 ± 0.05
57603.47215	18.85 ± 0.04
57607.42403	18.75 ± 0.04
57607.4755	18.73 ± 0.04
57608.42244	18.72 ± 0.04
57608.46314	18.76 ± 0.04
57610.37778	18.90 ± 0.05
57610.40956	18.90 ± 0.04
57614.27914	18.52 ± 0.04
57614.31513	18.54 ± 0.02
57621.48494	18.77 ± 0.08
57625.51741	18.71 ± 0.08

Table 2 continued

Table 2 *(continued)*

Date(MJD)	Mag
57627.49786	18.87 ± 0.05
57627.50277	18.83 ± 0.04
57630.48997	18.80 ± 0.04
57637.50613	18.67 ± 0.04
57637.52178	18.79 ± 0.08
57643.49325	18.66 ± 0.03
57643.51429	18.68 ± 0.03
57655.28962	18.88 ± 0.06
57657.31213	18.71 ± 0.04
57660.32479	18.71 ± 0.03
57666.32325	18.86 ± 0.05
57673.20179	18.50 ± 0.03
57681.27201	18.87 ± 0.05
57734.08192	18.61 ± 0.03
57737.08603	18.63 ± 0.06
57737.10603	18.58 ± 0.06
57741.07583	18.45 ± 0.04
57741.091	18.52 ± 0.05
57798.12369	18.58 ± 0.05

Table 3. g-band Photometry

Date(MJD)	Mag
55068.47442	19.46 ± 0.03
55182.10499	20.08 ± 0.03
55182.14066	20.18 ± 0.04
55182.17708	20.08 ± 0.04
55182.24007	20.25 ± 0.09
55182.27529	20.11 ± 0.07
55182.31123	19.95 ± 0.07
55182.34787	20.10 ± 0.10
56578.38672	20.16 ± 0.04
56578.42594	20.11 ± 0.04
56650.12354	20.07 ± 0.10
56655.10223	20.08 ± 0.08
56655.13466	20.09 ± 0.06
56657.09685	19.57 ± 0.05
56657.13672	19.45 ± 0.03
56907.24814	20.22 ± 0.11
56913.47892	20.30 ± 0.09

Table 3 continued

Table 3 *(continued)*

Date(MJD)	Mag
56913.51227	20.34 ± 0.07
56920.49168	18.17 ± 0.07
56920.5219	19.67 ± 0.07
56925.48542	20.32 ± 0.08
56925.51464	19.68 ± 0.07
56935.4322	20.17 ± 0.03
56936.38448	20.15 ± 0.09
56936.41448	20.52 ± 0.11
56940.39396	20.33 ± 0.11
56941.40683	19.97 ± 0.10
56944.36186	20.26 ± 0.07
56944.39101	20.30 ± 0.07
56946.37385	19.86 ± 0.05
56946.40318	20.24 ± 0.08
56949.35029	20.07 ± 0.05
56949.37965	20.07 ± 0.04
56950.34933	20.11 ± 0.02
56950.38148	19.92 ± 0.13
56951.36521	20.03 ± 0.04
56951.39894	19.90 ± 0.06
56952.35101	20.04 ± 0.03
56952.37968	20.14 ± 0.04
56953.34565	20.17 ± 0.05
56954.36273	20.31 ± 0.05
56954.39161	20.34 ± 0.04
56955.34692	20.32 ± 0.06
56955.37579	20.39 ± 0.08
56958.34337	20.32 ± 0.05
56965.194	20.42 ± 0.37
57255.32787	18.93 ± 0.19
57255.37765	18.81 ± 0.10
57256.3263	20.45 ± 0.08
57257.31646	20.30 ± 0.10
57257.35243	18.95 ± 0.13
57258.31311	19.11 ± 0.11
57270.40806	20.25 ± 0.06
57270.43794	20.45 ± 0.14
57271.40752	20.38 ± 0.07
57271.4372	20.59 ± 0.07
57286.28075	20.47 ± 0.06
57286.3111	20.36 ± 0.03
57655.44814	20.50 ± 0.16
57657.36159	20.20 ± 0.06

Table 3 continued

Table 3 *(continued)*

Date(MJD)	Mag
57660.37301	20.19 ± 0.04
57666.37122	20.44 ± 0.06
57673.16652	20.30 ± 0.10
57681.22238	20.24 ± 0.12
57763.10123	20.25 ± 0.21

REFERENCES

Barziv, O., Kaper, L., Van Kerkwijk, M. H., Telting, J. H., & Van Paradijs, J. 2001, A&A, 377, 925

Bildsten, L., Chakrabarty, D., Chiu, J., et al. 1997, ApJS, 113, 367

Bonanos, A.Z., Massa, D.L., Sewilo, M., et al. 2009, AJ, 138, 1003

Bouret, J.-C., Lanz, T., & Hillier, D. J. 2005, A&A, 438, 301

Boyer, M.L., McQuinn, B.W., Barmby, P., et al. 2015, ApJS, 216, 10

Bozzo, E., Falanga, M., Stella, L. 2008, ApJ, 683, 1031

Chaty, S. 2014, ASR, 52, 2132

Clark, J. S., Negueruela, I., 2004, A&A, 413, L15

Cohen, M., Kuhi, L. V., & Barlow, M. J. 1975, A&A, 40, 291

Cutri, R.M., Skrutskie, M.F., Van Dyk, S., et al. 2008, Explanatory Supplement to the 2MASS All Sky Data Release and Extended Mission Products (Pasadena, CA: IPAC)

Davidson, K., Ostriker, J.P. 1973, ApJ, 179, 585

Draine, B.T., Lee, H.M. 1984, ApJ, 285, 89

Draine, B. T. 2011, Physics of the Interstellar and Intergalactic Medium by Bruce T. Draine. Princeton University Press, 2011. ISBN: 978-0-691-12214-4,

Drave, S.P., Bird, A.J., Sidoli, L., et al. 2014, MNRAS, 439, 2175

Ducci, L., Doroshenko, V., Romano, P., et al. 2014, A&A, 568, A76

Fuchs, Y., Miramond L. K., Ábrahám, P. 2006, A&A, 445, 1041

Goldman et al. (in preparation)

Giménez-García, A., Shenar, T., Torrejón, J. M., et al. 2016, A&A, 591, A26

Groh, J. H., Damineli, A., Jablonski, F. 2007, A&A, 465, 993

Groh, J. H., Hillier, D. J., Damineli, A., et al. 2009, ApJ, 698, 1698

Groh, J. H., Damineli, A., Hillier, D. J., et al. 2009, ApJL, 705, L25

Hiltner, W. A., Werner, J., & Osmer, P. 1972, ApJL, 175, L19

Humphreys, R. M., Weis, K., Davidson, K., Bomans, D. J., & Burggraf, B. 2014, ApJ, 790, 48

Humphreys, R. M., Gordon, M. S., Martin, J. C., Weis, et al. 2017, ApJ, 836, 64

Illarionov, A.F., Sunyaev, R.A. 1974, A&A, 39, 185

Lamers, H. J. G. L. M., van den Heuvel, E. P. J., & Petterson, J. A. 1976, A&A, 49, 327

Lau, R. M., Kasliwal, M. M., Bond, H.E., et al. 2016, ApJ, 830, 142

Laycock, S., Cappallo, R., Oram, K., et al. 2014, ApJ, 789, 64

Liu, Q.Z., Paradijs, J. van, van den Huevel, E.P.J. 2001, A&A, 368, 1021

Masci, F. J., Laher, R. R., Rebbapragada, U. D., et al. 2017, PASP, 129, 014002

Monard, L.A.G. 2010, Central Bureau Electronic Telegrams, 2289, 1

Negueruela, I., Torrejón, J.M., Reig, P., et al. 2008, in A Population Explosion: The Nature and Evolution of X-ray Binaries in Diverse Environments, eds. R.M. Bandyopadhyay, S. Wachter, D. Gelino, and C.R. Gelino, AIP Conf. Ser., 1010, 256

Ofek, E. O., Sullivan, M., Shaviv, N.J., et al. 2014, ApJ, 789, 104

Oskinova, L. M., Hamann, W.-R., & Feldmeier, A. 2007, A&A, 476, 1331

Oskinova, L.M., Feldmeier, A., Kretschmar, P. 2012, MNRAS, 421, 2820

Quaintrell, H., Norton, A. J., Ash, T. D. C., et al. 2003, A&A, 401, 313

Romano, P., Krimm, H. A., Palmer, D. M., et al. 2014, A&A, 562, A2

Sako, M., Liedahl, D. A., Kahn, S. M., & Paerels, F. 1999, ApJ, 525, 921

Sidoli, L., Romano, P., Mereghetti, S., et al. 2007, A&A, 476, 1307

Sidoli, L. 2013, arXiv:1301.7574

Smith, N. 2014, ARA&A, 52, 487

Thöne, C. C., de Ugarte Postigo, A., Leloudas, G., et al. 2017, A&A, 599, A129

Vink, J.S. 2012, Eta Carinae and the Supernova Imposters, Astrophysics and Space Science Library, Vol 384

Walter, R., Zurita Heras, J. 2007, A&A, 476, 335

Wilson, J. C., Eikenberry, S. S., Hayward, T. L., et al. 2003, Proceedings of the SPIE, Vol 4841, 451-458.

de Wit, W. J., Oudmaijer, R. D., & Vink, J. S. 2014, Advances in Astronomy, 2014, 270848

Wright, A. E., Barlow, M. J. 1975, MNRAS, 170, 41